JACS
JOURNAL OF THE AMERICAN CHEMICAL SOCIETY
pubs.acs.org/JACS
Article

Vertically Stacked Boron Nitride/Graphene Heterostructure for Tunable Antiresonant Hollow-Core Fiber

Yi Cheng,* Xu Cheng, Jin Xie, Guang Cui, Shuting Cheng, Xiao Li, Jiajie Gan, Han Dong, Yuyao Yang, Wentao Yu, Ke Chen, Hao Hong, Xu Zhou, Meng Pang, Xin Jiang, Zhipei Sun,* Kaihui Liu,* and Zhongfan Liu*

Cite This: J. Am. Chem. Soc. 2025, 147, 33735−33742

Read Online

ACCESS | Metrics & More | Article Recommendations | Supporting Information

ABSTRACT: Incorporating atomically thin two-dimensional (2D) materials with optical fibers expands their potential for optoelectronic applications. Recent advancements in chemical vapor deposition have enabled the batch production of these hybrid fibers, paving the way for practical implementation. However, their functionality remains constrained by the integration of a single 2D material, restricting their versatile performance. Here, we introduce a boron nitride/graphene (BN/Gr) heterostructure in the antiresonant hollow-core fiber (ARF) to modulate its optical resonance and thus enhance graphene nonlinearity by controlling the BN thickness. Hydroxyl-rich methanol is employed to improve the flatness and crystallinity of graphene, promoting the vertical epitaxy of BN with a controllable thickness ranging from 5 to 50 nm. The engineered optical resonance notably tunes the light−graphene interaction within the BN/Gr-ARF, increasing the depth of nonlinear optical modulation from 4% to 10% and enhancing all-optical modulation performance by 75%. Our methodology opens possibilities for tunable optical waveguides via the direct growth of functional 2D material-based heterostructures, offering a robust platform for the development of highly integrated photonic devices.

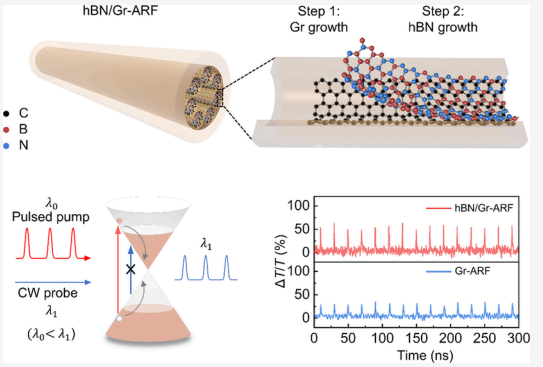

INTRODUCTION

Antiresonant hollow-core fibers (ARFs) advance light guidance by exploiting optical antiresonances across a broad wavelength range, particularly via a nested nodeless lattice of thin silica tubes as the cladding.[1,2] This unique structure offers ARFs superior optical performances over conventional optical fibers, including ultralow transmission loss and high transmission speed, reshaping optical communication.[3−7] Additionally, ARFs facilitate the development of diverse integrated all-fiber devices by tuning optical resonance through fiber redesign and redrawing or by filling the core with functional gases, enabling applications ranging from filters and frequency combs to quantum sources.[8−13] However, both approaches are often hindered by either remanufacturing complexity and limited accuracy or environmental instability and incompatibility with the established silica fiber platform.

The integration of solid-state two-dimensional (2D) nanomaterials with ARFs presents a promising alternative.[14−19] Previous research has demonstrated the potential of embedding single 2D materials into microstructured optical fibers to expand their optoelectronic applications.[20−24] However, their atomic-scale thickness contributes minimally to tuning ARF optical resonance, while increasing their thickness to a functional level compromises their intrinsic superior properties or induces strong light absorption, leading to undesirable transmission loss.[25] Hexagonal boron nitride (hBN), with a large and stable bandgap on thickness increase (∼6.0 eV, corresponding to light transparency >207 nm),[12,26] emerges as an ideal candidate for ARF integration to modulate its optical resonance. This tunability can be further leveraged to optimize light−matter interaction when paired with other functional 2D materials,[27] offering flexibility for developing compatible and versatile all-fiber devices.

Here, we vertically stacked an hBN/graphene heterostructure in the air-holes of ARF (hBN/Gr-ARF) using a sequential chemical vapor deposition (CVD) process. By introducing hydroxyl-rich methanol as a modifier, graphene adlayers were effectively suppressed, resulting in a smoother surface that enabled uniform and controllable hBN layer deposition. This tunability allowed for substantial adjustment of the optical resonance and enhanced light−graphene interaction within the ARF. Consequently, the nonlinear optical modulation depth of the hBN/Gr-ARF demonstrated a notable increase from ∼4%

Received: June 8, 2025
Revised: August 26, 2025
Accepted: August 27, 2025
Published: September 9, 2025

https://doi.org/10.1021/jacs.5c09658
J. Am. Chem. Soc. 2025, 147, 33735−33742

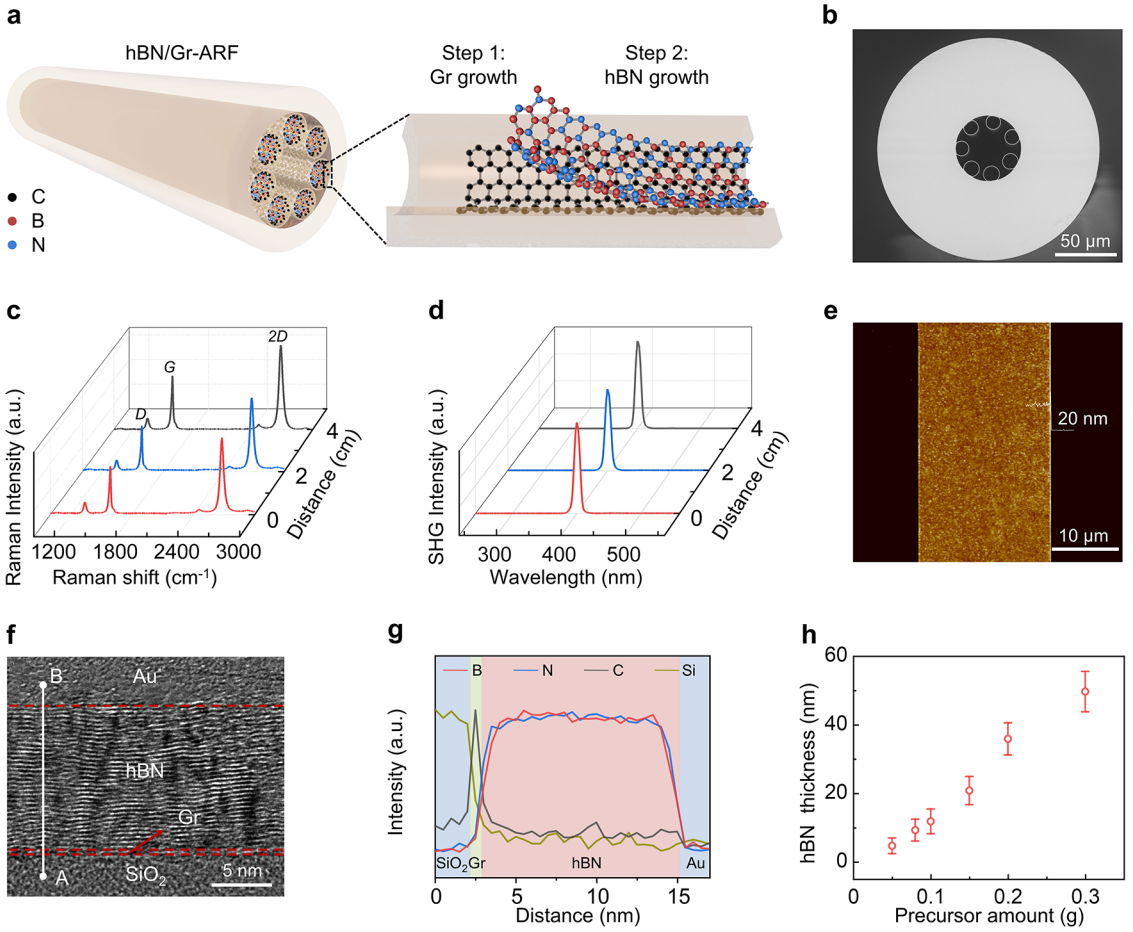

Figure 1. Growth of the hBN/Gr heterostructure on ARF. (a) Schematic of the two-step growth of the hBN/Gr heterostructure on ARF. (b) Cross-section SEM image of hBN/Gr-ARF. (c) Raman spectra of hBN/Gr-ARF at different positions along the fiber axis. (d) SHG signals at different positions along the fiber axis. (e) AFM image of the hBN/Gr ribbon after etching ARF. (f) Cross-section TEM image of the hBN/Gr-ARF. The regions of ARF, graphene (Gr), hBN, and gold (Au) protection layer are labeled, respectively. (g) EELS line scan analysis along the white line in f from point A to B. (h) hBN thickness varied with the input amounts of BH_3NH_3 precursors. The error bar here denotes standard deviations where $N = 3$.

to ~10%, while an all-optical modulator was further achieved with ~75% performance enhancement.

RESULTS AND DISCUSSION

hBN/Gr Heterostructure Growth on ARF. In our experiments, the growth of the hBN/Gr heterostructure was synthesized by sequentially depositing graphene and hBN layers on the ARF surface (Figure 1a). During the graphene growth, methane was used as the carbon precursor, with methanol vapor introduced as a growth modifier. In the subsequent step, ammonia borane (BH_3NH_3) was sublimated at ~90 °C for hBN growth (Figures S1 and S2). After the heterostructure deposition, the ARF preserved its original structure integrity, including the intact hollow core and periodic air-holes (Figure 1b and Figure S3). The darker optical contrast of hBN/Gr-ARF compared to that of Gr-ARF and bare ARF preliminarily suggested enhanced light absorption by graphene in the presence of hBN, since hBN is transparent to visible light (Figure S4). For graphene characterization, the graphene layer was solely deposited on the ARF without subsequent hBN layers. Raman spectra along the fiber axis confirmed the uniform growth of high-quality graphene by sharp G- and 2D-peaks and a low D- to G-mode intensity ratio (I_D/I_G) of ~0.2 (Figure 1c). After etching the silica fiber, the graphene within the air-holes collapsed into a compact ribbon, revealing its conformal coverage along the fiber air-holes (Figure S5a). Transmission electron microscopy (TEM) further verified the single-layer feature of the as-synthesized graphene (Figure S5b).

After the sequential growth of hBN, the successful deposition was confirmed by distinct B and N signals in X-ray photoelectron spectra (XPS, Figure S6) and the presence of a B−N signal (~1370 cm^{-1}) in infrared spectra (IR, Figure S7). Second harmonic generation (SHG) signals along the fiber axis further validated the uniformity of the as-synthesized hBN (Figure 1d), as the centrosymmetric graphene lattice does not contribute to SHG signals. Upon etching the silica fiber, a continuous hBN/Gr ribbon was obtained, displaying uniform distributions of B, N, and C signals with negligible O signal in energy dispersive X-ray spectroscopy (EDS) mapping, indicating high uniformity and purity of the heterostructure (Figure S8). The hBN thickness was determined by subtracting the graphene ribbon thickness (~2 nm, Figure S5a) from the total thickness of the hBN/Gr ribbons (Figure 1e and Figure S9) and then dividing the result by two.[28] A cross-sectional TEM image revealed well-aligned layered structures of graphene and hBN along the fiber axis (Figure 1f). Corresponding electron energy loss spectra (EELS) line

https://doi.org/10.1021/jacs.5c09658
J. Am. Chem. Soc. 2025, 147, 33735−33742

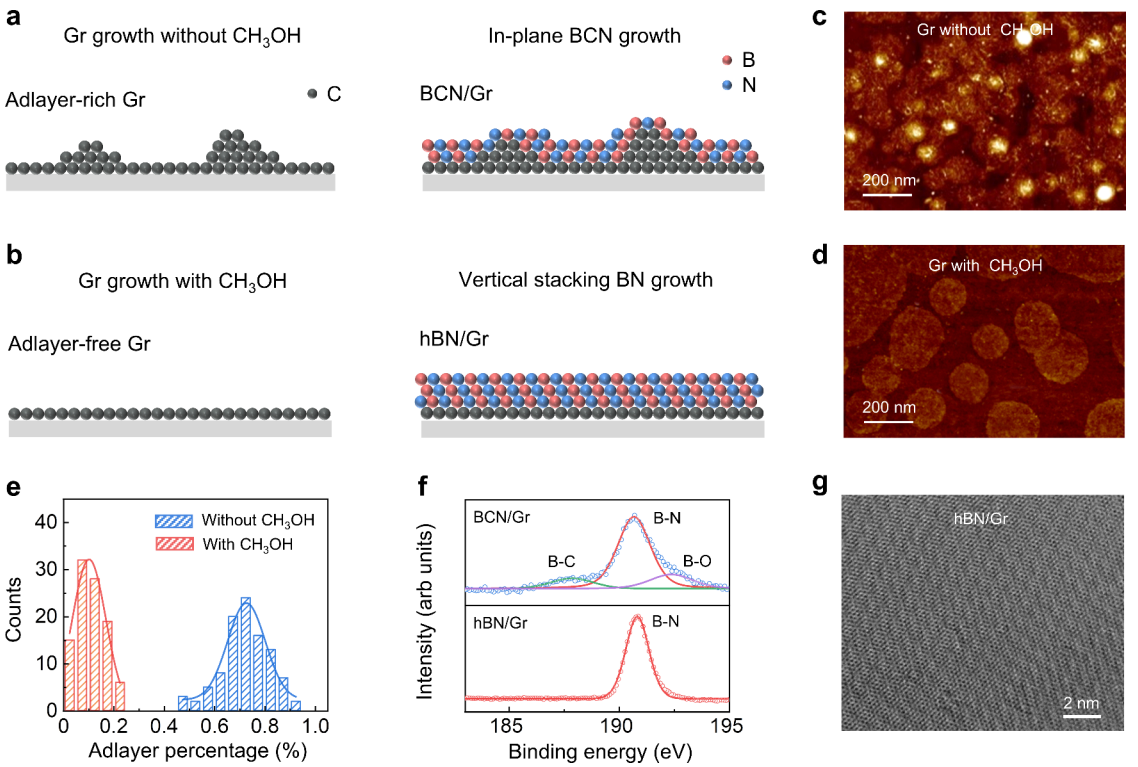

Figure 2. Control of the hBN/Gr stacking structure on ARF. (a) Schematic of BCN/Gr synthesis. BN tends to attach to the edge of the graphene adlayer and form the in-plane structure. (b) Schematic of hBN/Gr synthesis. BN was vertically stacked on the adlayer-free graphene. (c, d) AFM image of the graphene domain on the surface of ARF without (c) and with methanol (d). (e) Graphene adlayer percentage distribution without (blue line) and with (red line) methanol. 100 data points were collected for each sample. (f) XPS B 1*s* spectra of BCN/Gr-ARF (top) and hBN/Gr-ARF (bottom). (g) HRTEM images of the hBN/Gr.

scanning and EDS elemental mapping demonstrated a clear interface between graphene and hBN, confirming the vertical stacking configuration of the hBN/Gr heterostructure in the air-holes of the ARF (Figure 1g and Figure S10). By variation of the input amount of BH_3NH_3 precursors, the hBN thickness was modulated from ∼5 to 50 nm (Figure 1h).

Stacking Control of hBN/Gr Heterostructure. During the hBN/Gr heterostructure synthesis, an in-plane hBN-Gr structure (denoted as BCN) tends to form, especially along the edges of graphene adlayers, due to the closely matched lattice structures between hBN and graphene (lattice mismatch of <2%).[29−33] This in-plane configuration increases light absorption and degrades the nonlinear optical performance of graphene.[25] Therefore, reducing graphene adlayers and enhancing graphene flatness may provide an effective approach for achieving precise control of the vertical stacking between graphene and hBN, thereby optimizing the optical performance of the hybrid fiber. Theoretically, at the graphene growth temperature (∼1100 °C), methanol decomposes into OH radicals, which can etch graphene defects and promote the uniform growth of monolayer graphene (Figure S11).[34] In our experiments, we found that introducing methanol via argon bubbling during graphene growth prominently reduced the defect density, especially the adlayer percentage (Figure 2a,b). Specifically, the graphene adlayer percentage decreased from 0.73 to 0.08 with the introduction of methanol (Figure 2c−e and Figure S12). Meanwhile, this process decoupled the interaction between graphene and ARF, enabling quasi-suspended uniform graphene growth on ARF, as indicated by the suppression of C−O and sp^3 C signals in the C 1*s* XPS spectra (Figure S13). Furthermore, a distinct red shift in the 2D and G peaks was observed in the Raman spectra of the as-synthesized graphene compared to that synthesized without methanol (Figure S14), indicating a reduced graphene−substrate interaction. In addition, to evaluate the influence of ambient exposure on graphene, we measured the Raman spectra of Gr-ARF and hBN/Gr-ARF synthesized under identical conditions. The G and 2D band positions were comparable at 1582 and 2680 cm^{-1}, respectively (Figure S15), indicating that ambient exposure induced negligible differences in graphene doping. This methanol-introducing approach also enhanced the graphene grain size and crystallinity, as confirmed by atomic force microscopy (AFM) and high-resolution TEM (HRTEM) (Figure 2c,d and Figure S16).

The improved graphene flatness facilitated the subsequent vertical stacking of hBN with an enhanced uniformity (Figure 2a,b). After the sequential BN deposition, XPS analysis revealed distinct B−O, B−C, and N−C peaks for hBN/Gr-ARF synthesized without methanol (denoted as BCN/Gr-ARF), indicating the presence of in-plane BCN. In contrast, for hBN/Gr-ARF synthesized with methanol, only a single B−N peak was observed in both B 1*s* and N 1*s* spectra for hBN/Gr-ARF (Figure 2f and Figure S17). HRTEM images showed a lattice distortion in BCN/Gr (Figure S18), whereas hBN/Gr exhibited a crystalline lattice structure with moiré patterns (Figure 2g), confirming the successful control of the vertical stacking structure with negligible interlayer doping. Consequently, hBN/Gr-ARF showed a stronger SHG signal and higher thermal stability compared with BCN/Gr-ARF (Figures S19 and S20).

Simulation of hBN/Gr in Modulating the Optical Resonance of ARF. The tunability of the stacked hBN

https://doi.org/10.1021/jacs.5c09658
J. Am. Chem. Soc. 2025, 147, 33735−33742

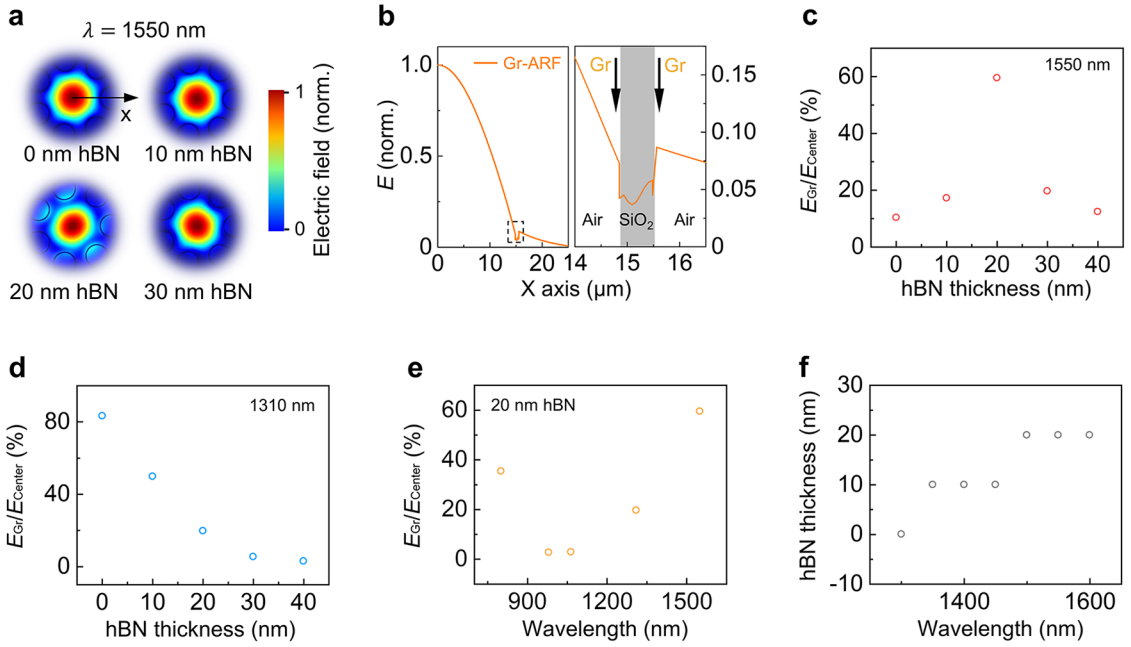

Figure 3. Simulation of tunable optical resonance in hBN/Gr-ARF. (a) Evolution of the fundamental mode in hBN/Gr-ARF at 1550 nm with varying hBN thicknesses. (b) Normalized electric field intensity distribution of monolayer graphene on ARF along the *X*-axis in a. The electric field intensity at the outer and inner graphene layer was ∼4.2% and 4.5%, respectively, to that at the core center, quantifying the light−graphene interaction along the fiber. (c) Ratio of the total electric field intensity at the two innermost graphene positions (as shown in b) to that at the core center (E_{Gr}/E_{Center}) varied with different hBN thicknesses at 1550 nm. (d) E_{Gr}/E_{Center} with different hBN thicknesses at 1310 nm wavelength. (e) E_{Gr}/E_{Center} at different laser wavelengths with 20 nm hBN showed a lower relative intensity within the 950−1100 nm range, indicating the antiresonance region. (f) Relationship between hBN thickness and wavelength at maximum E_{Gr}/E_{Center}.

thickness is expected to have a distinct impact on modulating the resonance behavior of the Gr-ARF.[1,2] To investigate this effect, we first conducted simulations to examine the evolution of the electric field in the hybrid fiber as the hBN thickness increased. Changes in the mode profile served as a visualized indicator for tracking shifts in the optical resonance of the hBN/Gr-ARF.[1,35] The simulation results revealed that at the telecommunication wavelength of 1550 nm, the fundamental mode of the hBN/Gr-ARF initially expanded as the hBN thickness increased from 0 to 20 nm and then contracted with a further increase to 40 nm (Figure 3a and Figure S21). It should be noted that the fundamental mode of an optical fiber possesses two degenerate polarization states because of the cylindrical symmetry of ARF. These polarization states became more strongly manifested when the optical resonance was distinctly enhanced with an hBN thickness of 20 nm, thereby giving rise to a pronounced mode asymmetry along the polarization direction (Figure S22). This variation influenced the distribution of electric field intensity within the fundamental mode, thus affecting the interaction between light and graphene.[20] To quantify this interaction, the intensity of the fundamental mode along the *X*-axis in the hybrid fiber was normalized (Figure 3b and Figure S23), and the ratio of E_{Gr}/E_{Center} was defined as the total electric field intensity at the two innermost graphene positions relative to that at the core center. The evolution of the other degenerated fundamental mode is also included in Figure S24, confirming that the following quantitative calculation of light−graphene interaction in Figure 3c was based on the combined influence of both fundamental modes. As the hBN thickness increased, E_{Gr}/E_{Center} followed a trend similar to that of the fundamental mode profile (Figure 3a) and peaked at ∼60% for an hBN thickness of 20 nm (Figure 3c), corresponding to the ARF optical resonance. In addition to hBN thickness, the input wavelength also influenced ARF optical resonance. When the wavelength was changed to another telecommunication band at 1310 nm, the fundamental mode showed a different evolution and became increasingly confined as the hBN thickness increased from 0 to 40 nm (Figure S25), consistent with the behavior of E_{Gr}/E_{Center} (Figure 3d). Across the wavelength range of 800 to 1600 nm, for an hBN thickness of 20 nm, E_{Gr}/E_{Center} reached a minimum value between 980 and 1064 nm (Figure 3e). This result closely aligned with the theoretical prediction regarding the optical resonance condition of the ARF (eq 1):

$$t = \frac{m\lambda}{2\sqrt{n_1^2 - n_0^2}} \tag{1}$$

where t is the tube thickness, λ is the wavelength, m is the resonance order represented by a positive integer, and n_1 and n_0 are the refractive index of the silica tube and air, respectively. Additionally, the hBN thickness corresponding to the maximum E_{Gr}/E_{Center} within the 1300 to 1600 nm wavelength range was analyzed, revealing a gradual increase with increasing wavelength (Figure 3f). This observation was consistent with the evolving trend of the resonance conditions in the ARF.

hBN/Gr-ARF-Based All-Optical Modulator. Experimentally, we found that the sole embedding of hBN introduced minimal additional loss (<0.02 dB cm^{-1}) to the bare ARF at wavelengths of 1550 and 1310 nm, owing to the large bandgap of hBN (Figure S26). This value remained stable, even when the peak intensity of the input light was increased to 50 MW cm^{-2}. In contrast, the hBN/Gr-ARF with an embedding hBN thickness of ∼20 nm exhibited a prominent transmission loss

https://doi.org/10.1021/jacs.5c09658
J. Am. Chem. Soc. 2025, 147, 33735−33742

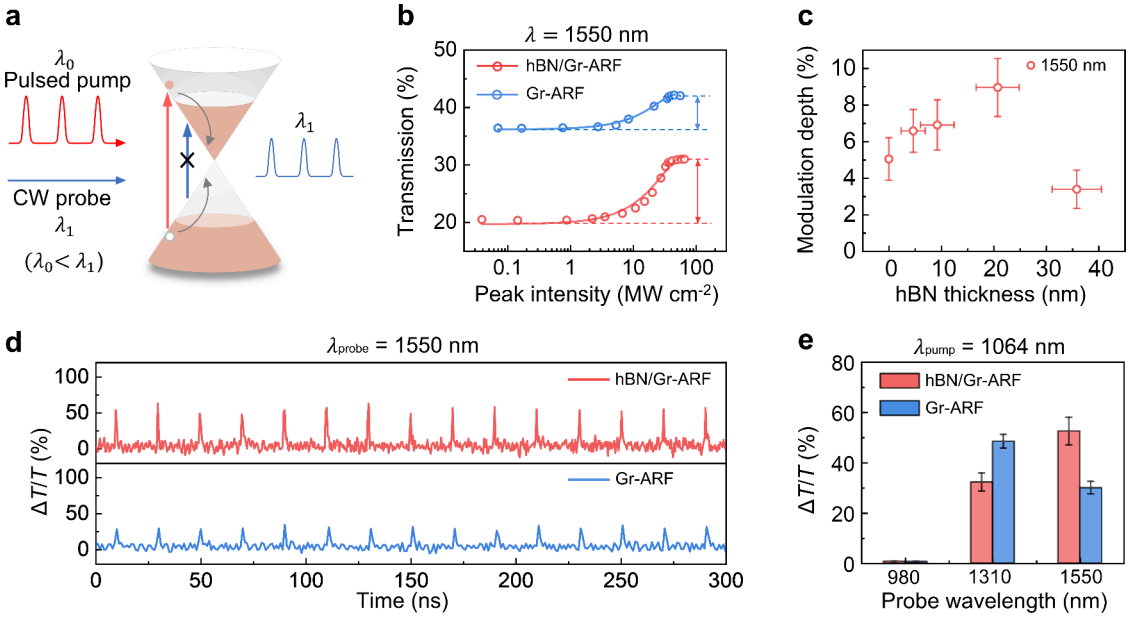

Figure 4. hBN/Gr-ARF-based all-optical modulator. (a) Schematic diagram of the all-optical modulation based on graphene nonlinear optical modulation. λ_0 and λ_1 represent the pulsed pump and CW probe light wavelengths, respectively. (b) Nonlinear optical modulation curves of hBN/Gr-ARF (with ~20 nm hBN thickness) and Gr-ARF. The solid curve was fitted according to the experimental data (circles). (c) Nonlinear optical modulation depth for the hBN/Gr-ARF at 1550 nm with different hBN thicknesses. (d) Modulated pulse train of 1550 nm CW probe light under a 1064 nm picosecond pump light in hBN/Gr-ARF with ~20 nm hBN thickness and Gr-ARF. ΔT is the change in transmission. (e) All-optical modulation performances of CW probe light at 980, 1310, and 1550 nm under a 1064 nm pulsed pump light. The error bars in parts c and e denote standard deviations, where $N = 3$.

of 0.55 dB cm^{-1}, which was 0.22 dB cm^{-1} higher than that of the Gr-ARF at 1550 nm (Figure S27). This increase indicated that the embedded hBN strengthened the light−graphene interaction in the ARF, driven by enhanced optical resonance. To exploit this effect for ARF-based integrated all-fiber devices, we first investigated the nonlinear optical modulation property of graphene (Figure 4a).[36] As the input light intensity increased, the transmission of the ARF gradually saturated, demonstrating a modulation depth of 9.8% in the hBN/Gr-ARF, compared to 4.1% in the Gr-ARF (Figure 4b). Furthermore, as the hBN thickness varied from 0 to ~35 nm, the modulation depth initially increased, with a peak at ~20 nm, and then declined (Figure 4c and Figure S28). This tunable behavior closely matched the trend observed in the simulation results in Figure 3a. When the pump wavelength was switched to 1310 nm, the modulation depth of the hBN/Gr-ARF showed a different dependence on the hBN thickness, decreasing consistently with the increase of hBN thickness (Figure S29). This outcome also aligned with the simulated evolution of the electric field distribution (Figure 3d) and suggested a transformation in light guidance from resonance to antiresonance conditions in the fiber. Notably, our vertical stacking control strategy, using methanol to minimize the graphene adlayers, played a vital role in enhancing the optical performance of the ARF. When comparing the modulation depths of BCN/Gr-ARF and hBN/Gr-ARF, both with similar graphene (monolayer) and BN/BCN thicknesses (~20 nm) and a pump wavelength at 1550 nm, the BCN/Gr-ARF exhibited a noticeable increase in transmission loss and a decrease in modulation depth compared to those of the hBN/Gr-ARF (Figure S30).

By leveraging graphene's ultrafast relaxation of photoexcited carriers,[37] the tunability of nonlinear optical modulation in hBN/Gr-ARF could potentially serve as a controllable and efficient all-optical modulator. When a pulsed pump at 1064 nm and a continuous wave (CW) probe at 1550 nm were launched into the hBN/Gr-ARF with a ~20 nm hBN thickness (Figure S31), the output CW light exhibited pronounced intensity modulation and a higher normalized pump-induced differential transmittance ($\Delta T/T$) of 52.6%, compared to 30.0% in the Gr-ARF, while maintaining the same repetition frequency as the pump light (Figure 4d). This improvement was attributed to the stronger resonance in the hBN/Gr-ARF. Both the hBN/Gr-ARF and Gr-ARF exhibited an ultrafast response on the order of ~0.20 ps under a 400 nm optical pump and an 800 nm optical probe (Figure S32). It is worth noting that the broader nanosecond time scale in Figure 4d, as compared to the subpicosecond time scale in Figure S32, was primarily limited by the bandwidth limitations of the photodetector and oscilloscope (MHz-GHz). In contrast, when the probe wavelength was shifted to 1310 nm, the hBN/Gr-ARF exhibited an ~16.2% lower $\Delta T/T$ compared to the Gr-ARF (Figure 4e). However, at a probe wavelength of 980 nm, $\Delta T/T$ became negligible in both the Gr/ARF and hBN/Gr-ARF, as carriers in the graphene valence band continued to absorb photons from the probe light, except at the states occupied by the longer-wavelength pump at 1064 nm (Figure 4e and Figure S33). The all-optical modulation capability of the hBN/Gr-ARF is not limited to modulating CW probes with pulsed lasers. A 1550 nm CW probe was also effectively modulated by a 980 nm CW pump light, achieving a comparable modulation depth of ~18% at a pump power of 450 mW (Figure S34). This all-optical modulation depth demonstrated a positive correlation with pump power, indicating a higher nonlinear optical response for the hBN/Gr-ARF.

https://doi.org/10.1021/jacs.5c09658
J. Am. Chem. Soc. 2025, 147, 33735−33742

CONCLUSIONS

In summary, we successfully synthesized a high-quality BN/Gr heterostructure in the air-holes of ARF using the CVD method. This hybrid BN/Gr-ARF demonstrated a strong capacity in engineering the fiber optical resonance by adjusting the thickness of the vertically stacked BN layer, thereby enhancing light−graphene interaction and notably improving the performance of an ultrafast all-optical modulator. The developed hBN/Gr heterostructure system exhibited other advantages over alternative 2D material heterostructures in terms of response time, operating wavelength range, fiber integrability, and environmental stability (Table S1). Extending this methodology to other 2D nanomaterials beyond BN and graphene, our strategy offers a versatile platform for modulating optical properties (such as dispersion, birefringence, and nonlinear coefficient) in structure-fixed waveguides across both linear and nonlinear regimes. This presents a promising route toward next-generation, compact, and integrable photonic devices for a wide range of applications.

ASSOCIATED CONTENT

Supporting Information

The Supporting Information is available free of charge at https://pubs.acs.org/doi/10.1021/jacs.5c09658.

Additional characterizations of Gr-ARF and hBN/Gr-ARF, simulations, electric field distribution, and nonlinear optical measurements (PDF)

AUTHOR INFORMATION

Corresponding Authors

Yi Cheng − *Center for Nanochemistry, Beijing Science and Engineering Center for Nanocarbons, Beijing National Laboratory for Molecular Sciences, College of Chemistry and Molecular Engineering, Peking University, Beijing 100871, China*; Email: chengyi-cnc@pku.edu.cn

Zhipei Sun − *QTF Center of Excellence, Department of Electronics and Nanoengineering, Aalto University, Espoo 02150, Finland*; orcid.org/0000-0002-9771-5293; Email: zhipei.sun@aalto.fi

Kaihui Liu − *State Key Laboratory for Mesoscopic Physics, Frontiers Science Center for Nano-optoelectronics, School of Physics and Academy for Advanced Interdisciplinary Studies, Peking University, Beijing 100871, China*; orcid.org/0000-0002-8781-2495; Email: khliu@pku.edu.cn

Zhongfan Liu − *Center for Nanochemistry, Beijing Science and Engineering Center for Nanocarbons, Beijing National Laboratory for Molecular Sciences, College of Chemistry and Molecular Engineering, Peking University, Beijing 100871, China; Beijing Graphene Institute (BGI), Beijing 100095, China*; orcid.org/0000-0003-0065-7988; Email: zfliu@pku.edu.cn

Authors

Xu Cheng − *QTF Center of Excellence, Department of Electronics and Nanoengineering, Aalto University, Espoo 02150, Finland; Group for Fiber Optics, École Polytechnique Fédérale de Lausanne (EPFL), Lausanne 1015, Switzerland*

Jin Xie − *State Key Laboratory for Mesoscopic Physics, Frontiers Science Center for Nano-optoelectronics, School of Physics and Academy for Advanced Interdisciplinary Studies, Peking University, Beijing 100871, China; Beijing Graphene Institute (BGI), Beijing 100095, China*

Guang Cui − *Center for Nanochemistry, Beijing Science and Engineering Center for Nanocarbons, Beijing National Laboratory for Molecular Sciences, College of Chemistry and Molecular Engineering, Peking University, Beijing 100871, China; Beijing Graphene Institute (BGI), Beijing 100095, China*

Shuting Cheng − *Beijing Graphene Institute (BGI), Beijing 100095, China; School of Population and Health, Renmin University of China, Beijing 100872, China*

Xiao Li − *Academy for Advanced Interdisciplinary Studies, Peking University, Beijing 100871, China*

Jiajie Gan − *Guangdong Basic Research Center of Excellence for Structure and Fundamental Interactions of Matter, Guangdong Provincial Key Laboratory of Quantum Engineering and Quantum Materials, School of Physics and Guangdong-Hong Kong Joint Laboratory of Quantum Matter, Frontier Research Institute for Physics, South China Normal University, Guangzhou 510006, China*

Han Dong − *Russell Center for Advanced Lightwave Science, Shanghai Institute of Optics and Fine Mechanics (SIOM) and Hangzhou Institute of Optics and Fine Mechanics (HIOM), Hangzhou 311400, China*

Yuyao Yang − *Center for Nanochemistry, Beijing Science and Engineering Center for Nanocarbons, Beijing National Laboratory for Molecular Sciences, College of Chemistry and Molecular Engineering, Peking University, Beijing 100871, China; Beijing Graphene Institute (BGI), Beijing 100095, China*

Wentao Yu − *Institute of Interdisciplinary Physical Sciences, School of Physics, Nanjing University of Science and Technology, Nanjing 210094, China*

Ke Chen − *Center for the Physics of Low-Dimensional Materials, School of Physics and Electronics, Henan University, Kaifeng 475004, China*; orcid.org/0000-0003-2384-8437

Hao Hong − *State Key Laboratory for Mesoscopic Physics, Frontiers Science Center for Nano-optoelectronics, School of Physics, Peking University, Beijing 100871, China*

Xu Zhou − *Guangdong Basic Research Center of Excellence for Structure and Fundamental Interactions of Matter, Guangdong Provincial Key Laboratory of Quantum Engineering and Quantum Materials, School of Physics and Guangdong-Hong Kong Joint Laboratory of Quantum Matter, Frontier Research Institute for Physics, South China Normal University, Guangzhou 510006, China*; orcid.org/0000-0003-3318-8735

Meng Pang − *Russell Center for Advanced Lightwave Science, Shanghai Institute of Optics and Fine Mechanics (SIOM) and Hangzhou Institute of Optics and Fine Mechanics (HIOM), Hangzhou 311400, China*

Xin Jiang − *Russell Center for Advanced Lightwave Science, Shanghai Institute of Optics and Fine Mechanics (SIOM) and Hangzhou Institute of Optics and Fine Mechanics (HIOM), Hangzhou 311400, China*

Complete contact information is available at: https://pubs.acs.org/10.1021/jacs.5c09658

Author Contributions

The manuscript was written through the contributions of all authors. These authors contributed equally: Y.C., X.C., J.X.

Notes

The authors declare no competing financial interest.

■ ACKNOWLEDGMENTS

This work was supported by the National Natural Science Foundation of China (T2188101, 52272032, 12427806, 52021006, 52272038, 52372046, 62375131), Beijing Municipal Science and Technology Commission (Z2211100-0450000), National Key R&D Program of China (2022YFA-1403500), and Natural Science Foundation of Jiangsu Province (BK20220947).

■ ABBREVIATIONS

hBN, hexagonal boron nitride; Gr, graphene; ARF, antiresonant hollow-core fiber; CW, continuous wave

■ REFERENCES

(1) Poletti, F. Nested Antiresonant Nodeless Hollow Core Fiber. *Opt. Express* **2014**, *22* (20), 23807−23828.
(2) Gao, S.-F.; Wang, Y.-Y.; Ding, W.; Jiang, D.; Gu, S.; Zhang, X.; Wang, P. Hollow-Core Conjoined-Tube Negative-Curvature Fibre with Ultralow Loss. *Nat. Commun.* **2018**, *9* (1), 2828.
(3) Mulvad, H.; Abokhamis Mousavi, S.; Zuba, V.; Xu, L.; Sakr, H.; Bradley, T.; Hayes, J.; Jasion, G.; Numkam Fokoua, E.; Taranta, A.; et al. Kilowatt-Average-Power Single-Mode Laser Light Transmission over Kilometre-Scale Hollow-Core Fibre. *Nat. Photonics* **2022**, *16* (6), 448−453.
(4) Taranta, A.; Numkam Fokoua, E.; Abokhamis Mousavi, S.; Hayes, J.; Bradley, T.; Jasion, G.; Poletti, F. Exceptional Polarization Purity in Antiresonant Hollow-Core Optical Fibres. *Nat. Photonics* **2020**, *14* (8), 504−510.
(5) Petrovich, M.; Fokoua, E.; Chen, Y.; Sakr, H.; Adamu, A.; Hassan, R.; Wu, D.; Ando, R.; Papadi, A.; Sandoghch, S.; et al. First Broadband Optical Fibre With an Attenuation Lower than 0.1 Decibel per Kilometre. *Nat. Photon.*, preprint, 2025, DOI: 10.1038/s41566-025-01747-5.
(6) Sakr, H.; Chen, Y.; Jasion, G. T.; Bradley, T. D.; Hayes, J. R.; Mulvad, H. C. H.; Davidson, I. A.; Numkam Fokoua, E.; Poletti, F. Hollow Core Optical Fibres with Comparable Attenuation to Silica Fibres between 600 and 1100 Nm. *Nat. Commun.* **2020**, *11* (1), 1−10.
(7) Osório, J. H.; Amrani, F.; Delahaye, F.; Dhaybi, A.; Vasko, K.; Melli, F.; Giovanardi, F.; Vandembroucq, D.; Tessier, G.; Vincetti, L.; et al. Hollow-Core Fibers with Reduced Surface Roughness and Ultralow Loss in the Short-Wavelength Range. *Nat. Commun.* **2023**, *14* (1), 1146.
(8) Wang, Q.; Wang, Z.; Zhang, H.; Jiang, S.; Wang, Y.; Jin, W.; Ren, W. Dual-Comb Photothermal Spectroscopy. *Nat. Commun.* **2022**, *13* (1), 2181.
(9) Zhao, P.; Zhao, Y.; Bao, H.; Ho, H. L.; Jin, W.; Fan, S.; Gao, S.; Wang, Y.; Wang, P. Mode-Phase-Difference Photothermal Spectroscopy for Gas Detection with an Anti-Resonant Hollow-Core Optical Fiber. *Nat. Commun.* **2020**, *11* (1), 847.
(10) Ni, W.; Yang, C.; Luo, Y.; Xia, R.; Lu, P.; Hu, D. J. J.; Danto, S.; Shum, P. P.; Wei, L. Recent Advancement of Anti-Resonant Hollow-Core Fibers for Sensing Applications. *Photonics* **2021**, *8* (4), 128.
(11) Sollapur, R.; Kartashov, D.; Zürch, M.; Hoffmann, A.; Grigorova, T.; Sauer, G.; Hartung, A.; Schwuchow, A.; Bierlich, J.; Kobelke, J.; et al. Resonance-Enhanced Multi-Octave Supercontinuum Generation in Antiresonant Hollow-Core Fibers. *Light Sci. Appl.* **2017**, *6* (12), e17124−e17124.
(12) Ma, K. Y.; Zhang, L.; Jin, S.; Wang, Y.; Yoon, S. I.; Hwang, H.; Oh, J.; Jeong, D. S.; Wang, M.; Chatterjee, S.; Kim, G.; Jang, A. R.; Yang, J.; Ryu, S.; Jeong, H. Y.; Ruoff, R. S.; Chhowalla, M.; Ding, F.; Shin, H. S. Epitaxial Single-Crystal Hexagonal Boron Nitride Multilayers on Ni (111). *Nature* **2022**, *606* (7912), 88−93.
(13) Tyumenev, R.; Hammer, J.; Joly, N.; Russell, P. S. J.; Novoa, D. Tunable and State-Preserving Frequency Conversion of Single Photons in Hydrogen. *Science* **2022**, *376* (6593), 621−624.
(14) Geim, A. K.; Novoselov, K. S. The Rise of Graphene. *Nat. Mater.* **2007**, *6* (3), 183−191.
(15) Splendiani, A.; Sun, L.; Zhang, Y.; Li, T.; Kim, J.; Chim, C.-Y.; Galli, G.; Wang, F. Emerging Photoluminescence in Monolayer MoS_2. *Nano Lett.* **2010**, *10* (4), 1271−1275.
(16) Caldwell, J. D.; Aharonovich, I.; Cassabois, G.; Edgar, J. H.; Gil, B.; Basov, D. Photonics with Hexagonal Boron Nitride. *Nat. Rev. Mater.* **2019**, *4* (8), 552−567.
(17) Xia, F.; Wang, H.; Xiao, D.; Dubey, M.; Ramasubramaniam, A. Two-Dimensional Material Nanophotonics. *Nat. Photonics* **2014**, *8* (12), 899−907.
(18) Autere, A.; Jussila, H.; Dai, Y.; Wang, Y.; Lipsanen, H.; Sun, Z. Nonlinear Optics with 2D Layered Materials. *Adv. Mater.* **2018**, *30* (24), No. 1705963.
(19) Loh, K. P.; Bao, Q.; Eda, G.; Chhowalla, M. Graphene Oxide as a Chemically Tunable Platform for Optical Applications. *Nat. Chem.* **2010**, *2* (12), 1015−1024.
(20) Chen, K.; Zhou, X.; Cheng, X.; Qiao, R.; Cheng, Y.; Liu, C.; Xie, Y.; Yu, W.; Yao, F.; Sun, Z.; Wang, F.; Liu, K.; Liu, Z. Graphene Photonic Crystal Fibre with Strong and Tunable Light−Matter Interaction. *Nat. Photonics* **2019**, *13* (11), 754−759.
(21) Zuo, Y.; Yu, W.; Liu, C.; Cheng, X.; Qiao, R.; Liang, J.; Zhou, X.; Wang, J.; Wu, M.; Zhao, Y.; Gao, P.; Wu, S.; Sun, Z.; Liu, K.; Bai, X.; Liu, Z. Optical Fibres with Embedded Two-Dimensional Materials for Ultrahigh Nonlinearity. *Nat. Nanotechnol.* **2020**, *15* (12), 987−991.
(22) Cheng, Y.; Yu, W.; Xie, J.; Wang, R.; Cui, G.; Cheng, X.; Li, M.; Wang, K.; Li, J.; Sun, Z.; et al. Controllable Growth of Graphene Photonic Crystal Fibers with Tunable Optical Nonlinearity. *ACS Photon.* **2022**, *9* (3), 961−968.
(23) Ngo, G. Q.; Najafidehaghani, E.; Gan, Z.; Khazaee, S.; Siems, M. P.; George, A.; Schartner, E. P.; Nolte, S.; Ebendorff-Heidepriem, H.; Pertsch, T.; et al. In-Fibre Second-Harmonic Generation with Embedded Two-Dimensional Materials. *Nat. Photonics* **2022**, *16* (11), 769−776.
(24) Xie, J.; Cheng, X.; Xue, G.; Li, X.; Zhong, D.; Yu, W.; Zuo, Y.; Liu, C.; Lin, K.; Liu, C.; et al. Critical-Layered MoS_2 for the Enhancement of Supercontinuum Generation in Photonic Crystal Fibre. *Adv. Mater.* **2024**, *36* (40), No. 2403696.
(25) Nair, R. R.; Blake, P.; Grigorenko, A. N.; Novoselov, K. S.; Booth, T. J.; Stauber, T.; Peres, N. M. R.; Geim, A. K. Fine Structure Constant Defines Visual Transparency of Graphene. *Science* **2008**, *320* (5881), 1308.
(26) Cassabois, G.; Valvin, P.; Gil, B. Hexagonal Boron Nitride is an Indirect Bandgap Semiconductor. *Nat. Photonics* **2016**, *10* (4), 262−266.
(27) Lin, Z.; McCreary, A.; Briggs, N.; Subramanian, S.; Zhang, K.; Sun, Y.; Li, X.; Borys, N. J.; Yuan, H.; Fullerton-Shirey, S. K.; et al. 2D Materials Advances: From Large Scale Synthesis and Controlled Heterostructures to Improved Characterization Techniques, Defects and Applications. *2D Mater.* **2016**, *3* (4), No. 042001.
(28) Cui, G.; Cheng, Y.; Liu, C.; Huang, K.; Li, J.; Wang, P.; Duan, X.; Chen, K.; Liu, K.; Liu, Z. Massive Growth of Graphene Quartz Fiber as a Multifunctional Electrode. *ACS Nano* **2020**, *14* (5), 5938−5945.
(29) Gao, T.; Song, X.; Du, H.; Nie, Y.; Chen, Y.; Ji, Q.; Sun, J.; Yang, Y.; Zhang, Y.; Liu, Z. Temperature-Triggered Chemical Switching Growth of in-Plane and Vertically Stacked Graphene-Boron Nitride Heterostructures. *Nat. Commun.* **2015**, *6*, 6835.
(30) Lu, G.; Wu, T.; Yang, P.; Yang, Y.; Jin, Z.; Chen, W.; Jia, S.; Wang, H.; Zhang, G.; Sun, J.; et al. Synthesis of High-Quality Graphene and Hexagonal Boron Nitride Monolayer in-Plane Heterostructure on Cu−Ni Alloy. *Adv. Sci.* **2017**, *4* (9), No. 1700076.
(31) Ci, L.; Song, L.; Jin, C.; Jariwala, D.; Wu, D.; Li, Y.; Srivastava, A.; Wang, Z. F.; Storr, K.; Balicas, L.; et al. Atomic Layers of Hybridized Boron Nitride and Graphene Domains. *Nat. Mater.* **2010**, *9* (5), 430−435.
(32) Liu, Z.; Ma, L.; Shi, G.; Zhou, W.; Gong, Y.; Lei, S.; Yang, X.; Zhang, J.; Yu, J.; Hackenberg, K. P.; et al. In-Plane Heterostructures of Graphene and Hexagonal Boron Nitride with Controlled Domain Sizes. *Nat. Nanotechnol.* **2013**, *8* (2), 119−124.

(33) Gong, Y.; Shi, G.; Zhang, Z.; Zhou, W.; Jung, J.; Gao, W.; Ma, L.; Yang, Y.; Yang, S.; You, G.; et al. Direct Chemical Conversion of Graphene to Boron- and Nitrogen- and Carbon-Containing Atomic Layers. *Nat. Commun.* **2014**, *5* (1), 3193.
(34) Wang, H.; Xue, X.; Jiang, Q.; Wang, Y.; Geng, D.; Cai, L.; Wang, L.; Xu, Z.; Yu, G. Primary Nucleation-Dominated Chemical Vapor Deposition Growth for Uniform Graphene Monolayers on Dielectric Substrate. *J. Am. Chem. Soc.* **2019**, *141* (28), 11004−11008.
(35) Hong, Y. F.; Gao, S. F.; Ding, W.; Zhang, X.; Jia, A. Q.; Sheng, Y. L.; Wang, P.; Wang, Y. Y. Highly Birefringent Anti-Resonant Hollow-Core Fiber with a Bi-Thickness Fourfold Semi-Tube Structure. *Laser Photonics Rev.* **2022**, *16* (5), No. 2100365.
(36) Lim, G.-K.; Chen, Z.-L.; Clark, J.; Goh, R. G.; Ng, W.-H.; Tan, H.-W.; Friend, R. H.; Ho, P. K.; Chua, L.-L. Giant Broadband Nonlinear Optical Absorption Response in Dispersed Graphene Single Sheets. *Nat. Photonics* **2011**, *5* (9), 554−560.
(37) Li, W.; Chen, B.; Meng, C.; Fang, W.; Xiao, Y.; Li, X.; Hu, Z.; Xu, Y.; Tong, L.; Wang, H.; et al. Ultrafast All-Optical Graphene Modulator. *Nano Lett.* **2014**, *14* (2), 955−959.

https://doi.org/10.1021/jacs.5c09658
J. Am. Chem. Soc. 2025, 147, 33735−33742